ARTICLE

High-Entropy Rock-Salt Surface Layer Stabilizes the Ultrahigh-Ni Single-Crystal Cathode

Zhongxing Xu,[⊥] Xinghan Chen,[⊥] Wenguang Fan,[⊥] Minzhi Zhan, Xulin Mu, Hongbin Cao, Xiaohu Wang, Haoyu Xue, Zhihai Gao, Yongzhi Liang, Jiajie Liu,* Xinghua Tan,* and Feng Pan*

ACCESS | Metrics & More | Article Recommendations | SI Supporting Information

ABSTRACT: Single-crystalline Ni-rich layered oxides are one of the most promising cathode materials for lithium-ion batteries due to their superior structural stability. However, sluggish lithium-ion diffusion kinetics and interfacial issues hinder their practical applications. These issues intensify with increasing Ni content in the ultrahigh-Ni regime ($\geq$90%), significantly threatening the practical viability of the single-crystalline strategy for ultrahigh-Ni layered oxide cathodes. Herein, by developing a high-entropy coating strategy, we successfully constructed an epitaxial lattice-coherent high-entropy rock-salt layer ($\sim$3 nm) via Zr and Al doping on the surface of the single-crystal cathode $LiNi_{0.92}Co_{0.05}Mn_{0.03}O_2$ through an *in situ* modification process. The surface high-entropy rock-salt layer with tailored Ni valence and lattice coherence not only greatly improves lithium-ion diffusion kinetics but also suppresses interface parasitic reactions and surface structural degradations. The high-entropy surface layer-stabilized ultrahigh-Ni single-crystalline cathode (SC-Ni92-ZA) demonstrates significantly improved rate and cycling performances (127.5 mAh g^{-1} at 20C, capacity retention of 74.9% after 500 cycles at 1C) in a half-cell. The SC-Ni92-ZA exhibits a capacity retention of 87.1% after 600 cycles at 1C in a full-cell. This epitaxial lattice-coherent high-entropy coating strategy develops a promising avenue for developing high-capacity, long-life cathode materials.

KEYWORDS: *layered oxide, single-crystalline cathodes, ultrahigh-Ni, high-entropy, lithium-ion batteries*
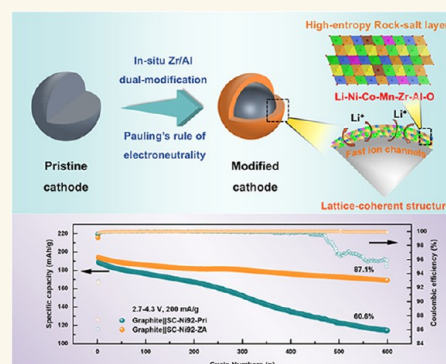
In recent years, the rapid development of the new energy industry—particularly in electric vehicles, consumer electronics, and grid storage—has driven a substantial demand for lithium-ion batteries with higher energy density and longer cycle life.[1−4] Among various candidates for the cathode, single-crystalline Ni-rich layered oxide with a nominal component of $LiNi_xCo_yMn_{1−x−y}O_2$ ($x > 0.6$, NCM) is regarded as one of the most promising cathode materials, owing to its high discharge specific capacity (>200 mAh g^{-1}), high operating voltage (>3.8 V), relatively low cost, excellent structural stability and safety.[5−8] To further meet the pursuit of high energy density, increasing the nickel content is a consistently effective approach in NCM cathode. Particularly, the ultrahigh-Ni NCM, symbolized by $LiNi_xCo_yMn_{1−x−y}O_2$ with $x \geq 0.9$, delivers a reversible capacity of more than 220 mAh g^{-1} under a 4.3 V cutoff voltage.[9] However, serious challenges, such as sluggish lithium-ion diffusion kinetics and interfacial issues, are dramatically exacerbated when using ultrahigh-Ni single crystals as cathodes. First, considering the sluggish lithium-ion diffusion kinetics, Sun et al. reported that by increasing the Ni content from 0.7 to 0.9 in NCM cathodes,

the discharge capacity discrepancy at 0.5 C between polycrystals and single crystals climbed from 10 to 26 mAh g^{-1}, and the gap in rate performance also widened significantly, rendering the ultrahigh-Ni single crystals almost unusable for practical applications.[10] Equally important, the long-term cycling stability of ultrahigh-Ni single crystals is severely compromised by interfacial issues, including interfacial side reactions, transition metal dissolution, and surface structure degradation, which stem from the high chemical activity of oxidized lattice oxygen $O^{\alpha-}$ ($\alpha < 2$) species and Ni^{4+} under high cutoff voltage.[11−14]

Recently, high-entropy strategies have been applied to the design of advanced materials, as high-entropy materials exhibit
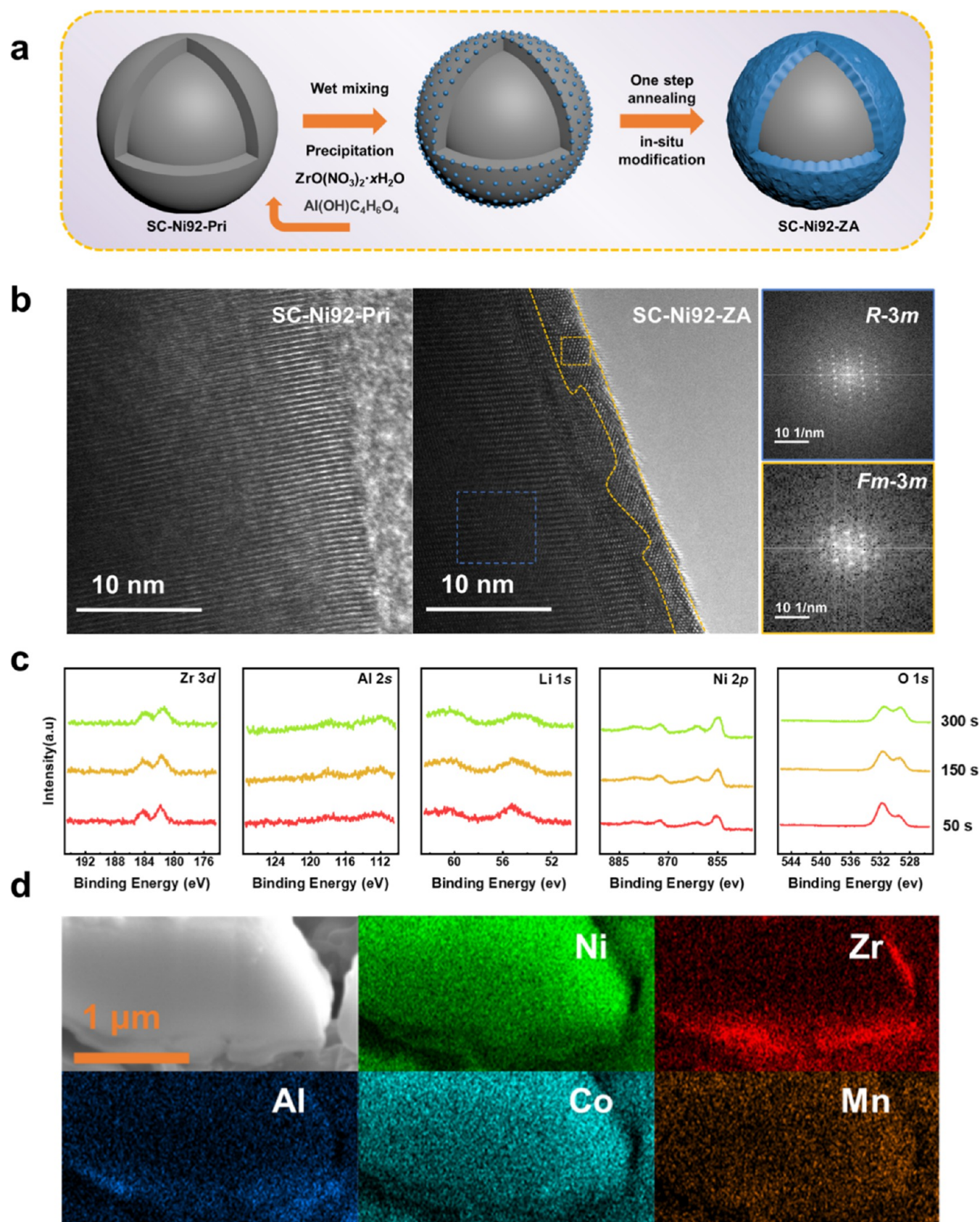
Figure 1. Modification strategy, morphology, and structural analysis of SC-Ni92-ZA. (a) Schematic diagram of the process to produce SC-Ni92-ZA; (b) HRTEM images of SC-Ni92-Pri and SC-Ni92-ZA; (c) In-depth XPS spectra of Zr 3d, Al 2s, Li 1s, Ni 2p, and O 1s for SC-Ni92-ZA powder; (d) EDS elemental mappings of Ni, Zr, and Al for the cross-section of SC-Ni92-ZA powder.

unique physical and chemical properties.[15−17] In accordance with the Gibbs−Helmholtz equation, the Gibbs free energy diminishes with increasing entropy, consequently imbuing high-entropy materials with superior and inherent stability.[18,19] Building on this understanding, it has been conclusively demonstrated that the stability and performance of cathode materials can be markedly improved through high-entropy stabilization or strategies inspired by it.[20−24] Nevertheless, given that high-Ni content is pivotal to achieving high capacity in ultrahigh-Ni single-crystalline cathodes, it is clear that the conventional near-equimolar strategy is unfeasible.[21,25] High-entropy surface modification is a potentially effective strategy[20,22,26] that significantly improves the stability of the interfacial structure while ensuring a substantial Ni content in the bulk. Additionally, the high-entropy surface layer can provide fast lithium-ion transport channels to improve diffusion kinetics when it is epitaxially lattice-coherent with the bulk material. For instance, Amine et al. utilized an epitaxial entropy-assisted coating strategy based on the crystallographic structural congruence between the Wadsley-Roth phase and layered-oxide cathodes to achieve fast ionic transport in ultrahigh-Ni polycrystals.[22] In our previous work, we constructed a coherent near-surface high-entropy zone by Mg−Al−Eu codoping to enhance the rate and cycling performance of $LiCoO_2$ at high voltage.[26] However, the construction of epitaxial lattice-coherent high-entropy surface layers in ultrahigh-Ni single crystals has rarely been reported systematically, and the fundamental design principles underlying this process have not been fully revealed.

Herein, inspired by the concept of high-entropy stabilization, we propose an innovative approach to construct an epitaxial high-entropy rock-salt structure on the surface of an ultrahigh-Ni single-crystalline cathode $LiNi_{0.92}Co_{0.05}Mn_{0.03}O_2$ (SC-Ni92-Pri) to address interfacial issues and sluggish lithium-ion diffusion kinetics. Based on Pauling's rule of electroneutrality, in a stable crystal structure, the sum of the strength of the electrostatic valence bonds of the nearest neighboring cations tends to equal the electric charge of the anion. Accordingly, for the ultrahigh-Ni single-crystal system, the relation of $Q = -2 + \sum_{i=1}^{6} Z_i/6$ (Z = electric charge of cations) should approach zero to ensure the stability of the octahedral coordination structure.[27,28] Consequently, the epitaxial high-entropy rock-salt structure can be successfully achieved through an *in situ* surface Zr/Al dual-modification process according to Pauling's rule of electroneutrality. The construction mechanism and enhancement effects of this structure can be attributed to the following aspects: (1) Modulating the Ni valence on the surface by the introduction of the high-valence Zr element owing to the electric charge compensation, facilitating the induction of a surface lattice-coherent rock-salt layer and stabilization of the interfacial structure by suppressing Ni valence on the surface at the high delithiation states;[29−31] (2) Strengthening the covalent bond between the transition metal and oxygen to further inhibit surface oxygen loss by introducing Al and Zr;[32,33] (3) Forming a lattice-coherent high-entropy rock-salt layer (Li−Ni−Co−Mn−Zr−Al−O) with Zr, Al and Li enrichment, which is considered potentially beneficial for Li-ion diffusion. Thus, the surface high-entropy coating-stabilized $LiNi_{0.92}Co_{0.05}Mn_{0.03}O_2$ cathode exhibits excellent rate and cycling performance under a 4.4 V cutoff voltage. This work highlights the great potential of the epitaxial lattice-coherent high-entropy rock-salt structure for ultrahigh-Ni single-crystalline cathode materials.

1. RESULTS AND DISCUSSION

The schematic diagram of the synthesis process for SC-Ni92-ZA was depicted in Figure 1a. As shown in Figure S1, Supporting Information, a well-defined single-crystalline morphology and smooth surfaces can be detected in both SC-Ni92-Pri and SC-Ni92-ZA, with particle sizes of approximately 2−3 μm. The elements were uniformly distributed in both samples, as revealed by scanning electron microscope (SEM) mapping images (Figures S2 and S3, Supporting Information). The Rietveld refinements of X-ray diffraction (XRD) patterns and the corresponding locally enlarged views of SC-Ni92-Pri and SC-Ni92-ZA are shown in Figure S4, Supporting Information, indicating that both samples exhibited an α-$NaFeO_2$-type hexagonal structure with an R-3m space group, with no impurities detected. The peaks of (006)/(012) and (018)/(110) split clearly, indicating well layered structures in both samples. The results of Rietveld refinements are listed in Tables S1 and S2, Supporting Information. Compared to SC-Ni92-Pri (14.18188 Å), the lattice parameter c of SC-Ni92-ZA (14.18543 Å) increased slightly, which may be attributed to the near-surface introduction of Zr^{4+} and Al^{3+} ions, resulting in the expansion of the interlayer spacing.

Leveraging high-resolution transmission electron microscope (HRTEM), the surface structures of the two materials were meticulously characterized at the atomic scale. In Figure 1b, a neat arrangement of layered structures without structural abnormality is observed at the surface of SC-Ni92-Pri. As for SC-Ni92-ZA, a lattice-coherent rock-salt layer (~3 nm) was constructed at the edge zone due to the *in situ* surface modification, as confirmed by the corresponding fast Fourier transform (FFT) image. To elucidate further details of the lattice-coherent layer in SC-Ni92-ZA, X-ray photoelectron spectroscopy (XPS) at various etching time was utilized to detect the element distribution and value states from the surface to the interior. As shown in Figure 1c, the signal intensity of Ni gradually increased from the surface to the interior, while the signal intensity of Li remained relatively constant. Notably, signals of exotic elements Zr and Al were detected during the etching process. These results reveal the concurrent enrichment and penetration of Zr and Al on the surface and near-surface region and confirm the composition of the disordered rock-salt layer as a Li−Ni−Co−Mn−Zr−Al−O-type high-entropy complex. Furthermore, energy dispersive spectrometer (EDS) elemental mappings acquired on the cross-section of SC-Ni92-ZA (prepared by focused ion beam) show that Zr and Al primarily segregate on the surface of SC-Ni92-ZA (Figure 1d). Considering no external coating layer was detected on the surface of SC-Ni-92-ZA (Figure 1b), it suggests Zr and Al elements were introduced into the lattice structure of the near-surface region. This particular composition of the surface high-entropy layer is potentially beneficial for Li-ion diffusion. First, the high valence state of Zr^{4+} and Al^{3+} (compared to Ni^{2+}) may introduce an abundance of Li ions to the rock-salt region, thereby constructing fast ion transport channels. Second, Zr and Al can penetrate the near-surface layered structure, enhancing lithium-ion diffusion kinetics. Last but not least, the lattice-coherent connection of the bulk and surface structure may reduce lithium-ion diffusion barriers.
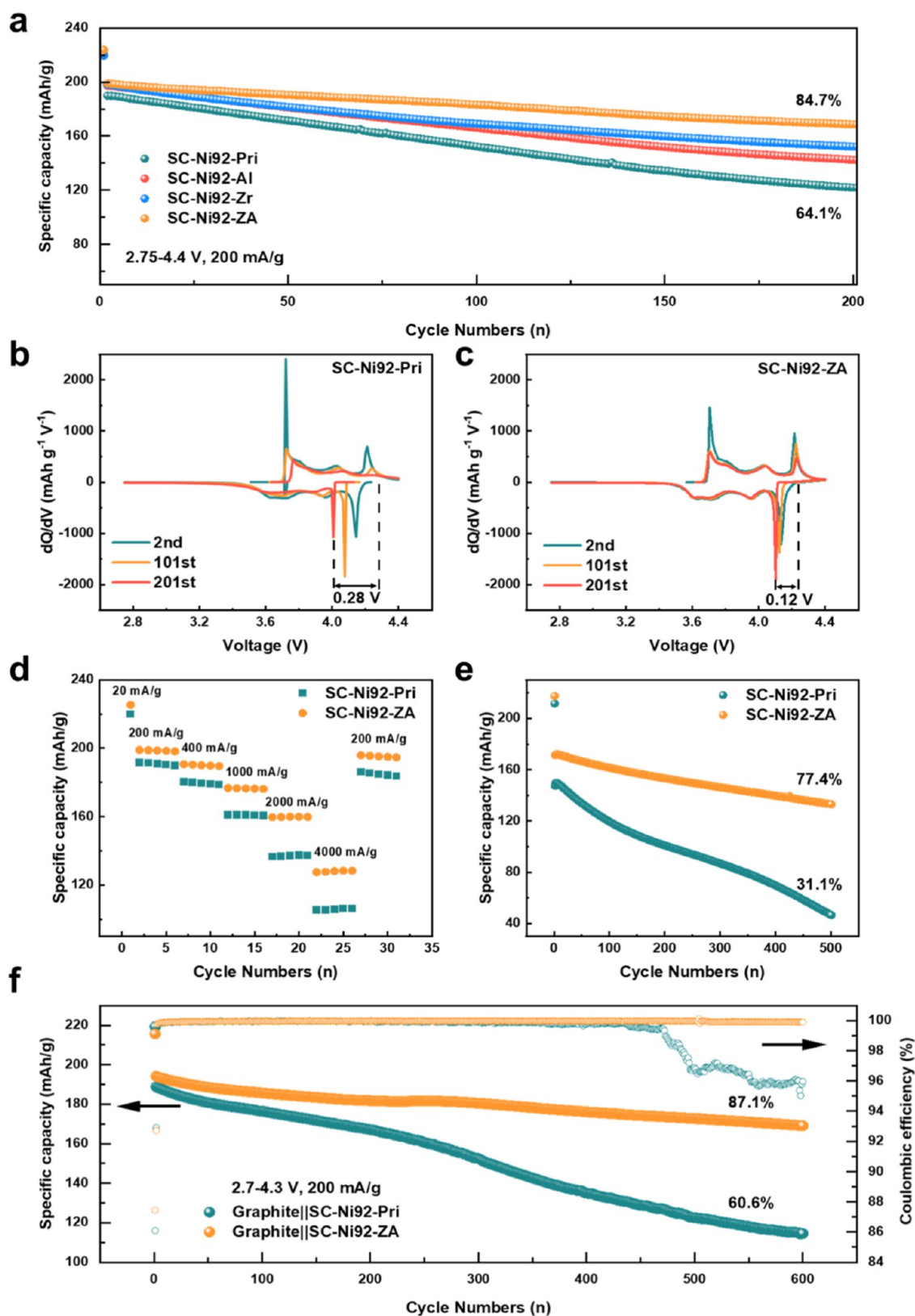
Figure 2. Electrochemical performance comparison. (a) Cycling performance of half-cells for SC-Ni92-Pri, SC−Ni92-Al, SC−Ni92-Zr, and SC-Ni92-ZA; (b-c) The corresponding dQ dV^{-1} curves; (d) Rate performance; (e) Cycling performance at 5C high rate; (f) Cycling performance of full cells with graphite as the anode at 1C and within the voltage range of 2.7−4.3 V.

In order to verify our design concept, SC-Ni92-Pri and SC-Ni92-ZA were subjected to cyclic voltammetry (CV) at different sweep rates to examine Li⁺ transport kinetics (Figure

S5a-b, Supporting Information). Both SC-Ni92-Pri and SC-Ni92-ZA underwent a sequence of redox processes and phase transitions, from H1 to M, to H2, and to H3 (where H and M

represent hexagonal and monoclinic, respectively).[34] According to the Randles-Sevcik equation, the peak current I_p and scan rate $v^{0.5}$ can be linearly fitted, with the slope being positively correlated with the lithium-ion diffusion coefficient (Figure S5c, Supporting Information).[35] Apparently, a higher slope value of 1.89 can be observed for SC-Ni92-ZA, compared to the 1.37 for SC-Ni92-Pri, suggesting enhanced lithium-ion diffusivity in the former. In addition, the much sharper redox peaks of SC-Ni92-ZA implied significantly improved ionic transport kinetics. Even at a low sweep rate (0.1 mV/s), SC-Ni-92-ZA exhibited lower polarization and sharper redox peaks than SC-Ni92-Pri (Figure S5d, Supporting Information). The role of the surface high-entropy layer was further investigated by using the Galvanostatic Intermittent Titration Technique (GITT) (Figure S6, Supporting Information). Based on the lithium-ion diffusion coefficients calculated from the GITT results (Figure S6c−d, Supporting Information), SC-Ni92-ZA exhibited superior ion kinetics compared to SC-Ni92-Pri throughout the cycling process.[36] Furthermore, after cycling, the divergence in lithium-ion diffusion coefficients between the two samples became more pronounced within the voltage range exceeding 4.2 V, indicating that the irreversible H2−H3 phase transition in SC-Ni92-Pri resulted from reduced lithium-ion diffusion kinetics. These results demonstrate a significant enhancement in lithium-ion diffusion kinetics, redox reversibility and depolarization, achieved by the epitaxial lattice-coherent high-entropy rock-salt layer.

As depicted in Figure S7, Supporting Information, SC-Ni92-ZA exhibited an initial discharge specific capacity of 224.0 mAh g^{-1}, higher than that of SC-Ni92-Pri (220.3 mAh g^{-1}) at 0.1C (1C = 200 mA g^{-1}). The capacity difference was more evident at 1C, with SC-Ni92-ZA showing an approximate increase of 9.2 mAh g^{-1} in discharge capacity relative to SC-Ni92-Pri. The expanded capacity further validated the effectiveness of the surface high-entropy modification strategy in improving the lithium-ion kinetics of the ultrahigh-Ni single-crystal cathode. Furthermore, after 200 cycles, SC-Ni92-ZA maintained the highest capacity retention of 84.7%, outperforming SC−Ni92-Zr (∼76.7%, Zr-modified), SC−Ni92-Al (∼72.1%, Al-modified) and SC-Ni92-Pri (∼64.1%) (Figure 2a). After long-term cycling, SC-Ni92-ZA still exhibited excellent capacity retention (74.9%, 500 cycles) (Figure S8, Supporting Information). The charge−discharge and differential capacity (dQ dV^{-1}) curves during cycling, shown in Figure S9 and Figure 2b−c, respectively, indicate that surface high-entropy modification significantly improved the reversibility of the H2−H3 phase transition and markedly reduced polarization. SC-Ni92-ZA consistently demonstrated prominent discharge capacity, surpassing that of SC-Ni92-Pri, and the performance gap widened as the rate increased. Notably, as illustrated in Figure 2d, at a current density of 20C, SC-Ni92-ZA still delivered a discharge capacity of 127.5 mAh g^{-1}, whereas SC-Ni92-Pri exhibited only 105.4 mAh g^{-1}. Additionally, SC-Ni92-ZA demonstrated improved long-term cycling stability compared to SC-Ni92-Pri at a high rate, retaining 77.4% of its capacity after 500 cycles at 5C, while the latter remained only 31.1% (Figure 2e). Harsh condition electrochemical performance is vital to battery applications.[37] Notably, in comparison to the SC-Ni92-Pri, SC-Ni92-ZA exhibited not only a higher capacity release but also superior cycling stability under challenging conditions (Figure S10, Supporting Information). Moreover, SC-Ni92-ZA retained a reversible discharge capacity of 169.0 mAh g^{-1} with a capacity retention of 87.0% after 600

cycles in full-cell. In contrast, SC-Ni92-Pri's full-cell retained only 114.5 mAh g^{-1}, with a retention rate of 60.5% (Figure 2f). The electrochemical performances of SC-Ni92-ZA were highly competitive among ultrahigh-Ni single-crystalline cathode materials (Table S3, Supporting Information). The impact of the postheating process on electrochemistry performance (Figure S11, Supporting Information) has also been investigated, revealing that the outstanding performance primarily stems from surface modification rather than the postannealing treatment. Electrochemical properties of SC-Ni92-ZA at various sintering temperatures (Figure S12, Supporting Information) revealed that the optimal temperature for achieving the best results from surface high-entropy layer construction was 500 °C. This modification strategy was extended to improve single-crystal LiNi$_{0.83}$Co$_{0.12}$Mn$_{0.05}$O$_2$ (SC-Ni83) and polycrystalline LiNi$_{0.83}$Co$_{0.12}$Mn$_{0.05}$O$_2$ (PC-Ni83). The results (Figure S13, Supporting Information) confirmed the broad applicability of this modification strategy, as performance improvements were observed in both single-crystal and polycrystalline samples following surface modification.

Electrochemical Impedance Spectroscopy (EIS) was performed to investigate the interface-related properties (Figure S14, Supporting Information). The EIS spectra display two semicircles and an inclined line, corresponding to the cathode electrolyte interface (CEI) film resistance (R_f), charge transfer impedance (R_{ct}) and Warburg impedance (w_0), spanning from the high- to the low-frequency regions, respectively.[38] As shown in Table S4, SC-Ni92-Pri exhibited significantly higher R_{ct} values than SC-Ni92-ZA, particularly after long-term cycling. The impedance evolution was further studied using in situ EIS, as depicted in Figure S15, Supporting Information. While the values of R_f remained almost constant throughout the electrochemical processes, the R_{ct} values fluctuated widely at different states of charge (SOCs). Particularly, the SC-Ni92-ZA consistently maintained a significantly lower R_{ct} compared to SC-Ni92-Pri, demonstrating superior performance throughout the electrochemical process. Additionally, the advanced distribution of relaxation time (DRT) method was used to further analyze in situ EIS data (Figure S16, Supporting Information).[39−41] The area and characteristic time constant of the peaks were strongly correlated with impedance and kinetics processes. The peaks with a time range of 10^{-5}−10^{-4}, 10^{-4}−10^{-3}, and 0.1−10 s, can be attributed to R_s, R_f, and R_{ct}, respectively.[41] This clearly demonstrated that the sharply increased R_{ct} was the main contributor to impedance, leading to deteriorated kinetics and capacity.

Density functional theory (DFT) calculations were conducted to investigate the lattice oxygen stability and lithium-ion migration after near-surface doping with Al and Zr. As shown in Figures S17−18, Supporting Information, the introduction of Zr and Al ions led to an increase in oxygen vacancy formation energy, with the codoping of Zr and Al exhibiting the highest oxygen vacancy formation energy. Lithium-ion diffusion barriers were also compared at different SOCs (Figures S19−21, Supporting Information). Although the introduction of Zr/Al had a negligible influence on lithium-ion migration in the initial state of charge, it significantly reduced the diffusion barrier for lithium-ion migration after delithiation.

In situ XRD was performed to reveal the phase evolution during the first charge−discharge cycle from 2.75 to 4.4 V at 0.2C (Figure 3a−b). The position of the (003) diffraction peak
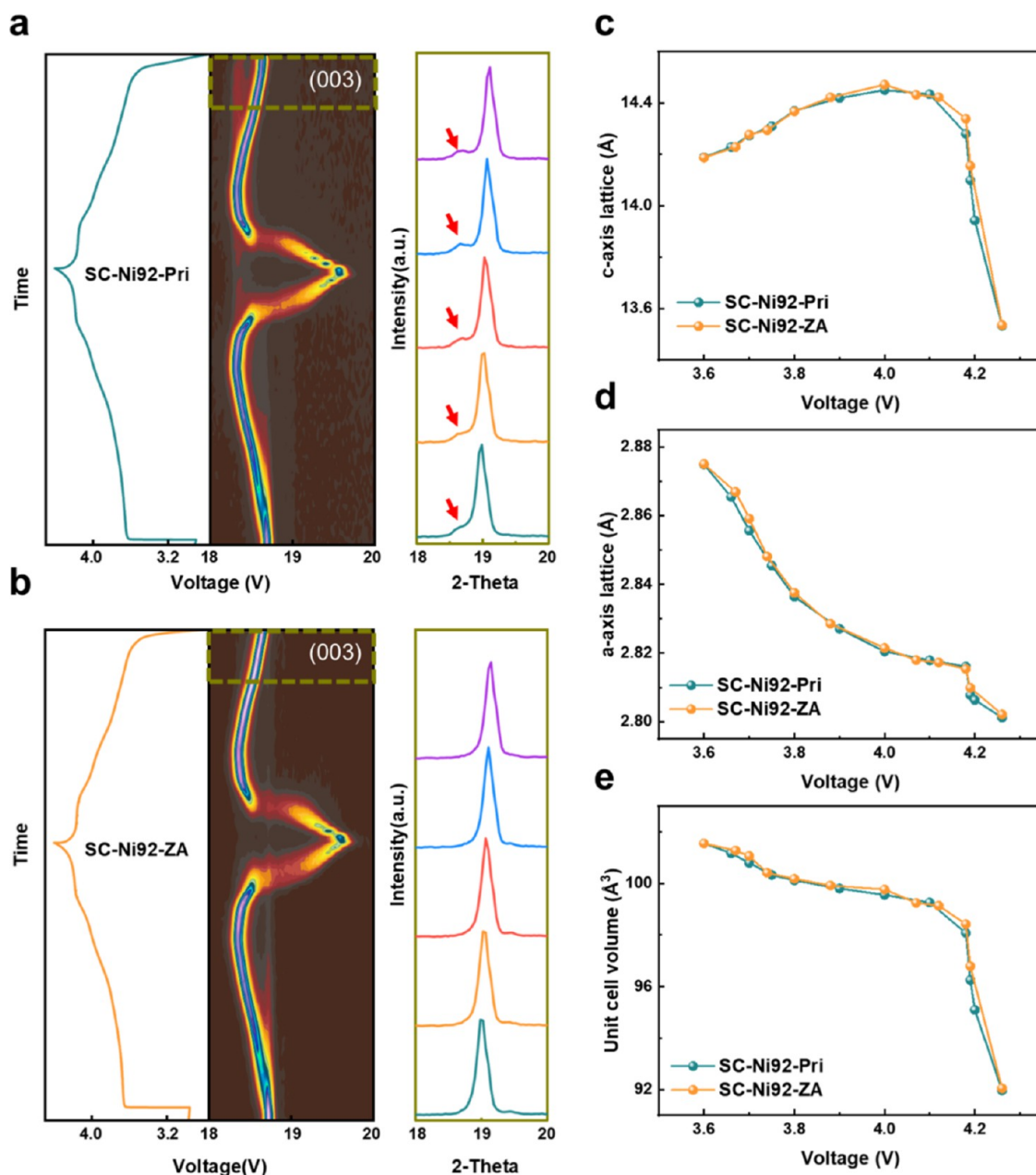
Figure 3. *In situ* XRD results and the corresponding enlarged views for (a) SC-Ni92-Pri and (b) SC-Ni92-ZA. For clear, the selected peaks were displayed to the right of (a) and (b); Lattice parameters of (c) *c*-axis lattice, (d) *a*-axis lattice, and (e) unit cell volume during the cycling process by Rietveld refinement calculation.

is closely related to the value of the *c*-axis.[42] As shown in Figure 3c−e, the lattice parameters of SC-Ni92-Pri and SC-Ni92-ZA were similar during the charging process. However, SC-Ni92-Pri showed an incomplete phase transition, with a residual H2 phase remaining at the end of discharge, whereas this was absent in SC-Ni92-ZA. Consequently, the surface high-entropy shell had no impact on the changes in the lattice parameters of the bulk phase during the charge/discharge process. The enhanced phase transition reversibility may stem from the improved Li⁺ transport kinetics of the epitaxial lattice-coherent high-entropy rock-salt layer.

Upon charging to a high voltage, the electrolyte undergoes oxidation due to the close proximity of the Fermi level of the cathodes to the highest occupied molecular orbital (HOMO) level of the electrolyte, coupled with an increased concen-

tration of holes.[43,44] Additionally, the dissolution of transition metals results in the generation of fluorides through side reactions with the electrolyte.[45,46] These processes lead to the formation of a complex and thick CEI film on the surface, thereby impeding the transport of lithium ions. The morphologies of SC-Ni92-Pri and SC-Ni92-ZA were observed using SEM after different cycles, as depicted in Figures S22−23, Supporting Information. Before the electrochemical cycle, the surfaces of the two samples were smooth and clean. After 200 cycles, the surface of SC-Ni92-Pri became rough, whereas that of SC-Ni92-ZA remained largely unchanged, indicating the formation of a thicker CEI film in the former. Additionally, due to suppressed oxygen evolution in SC-Ni92-ZA, the formation of detrimental microcracks was also avoided. XPS was performed to reveal the chemical compositions of the
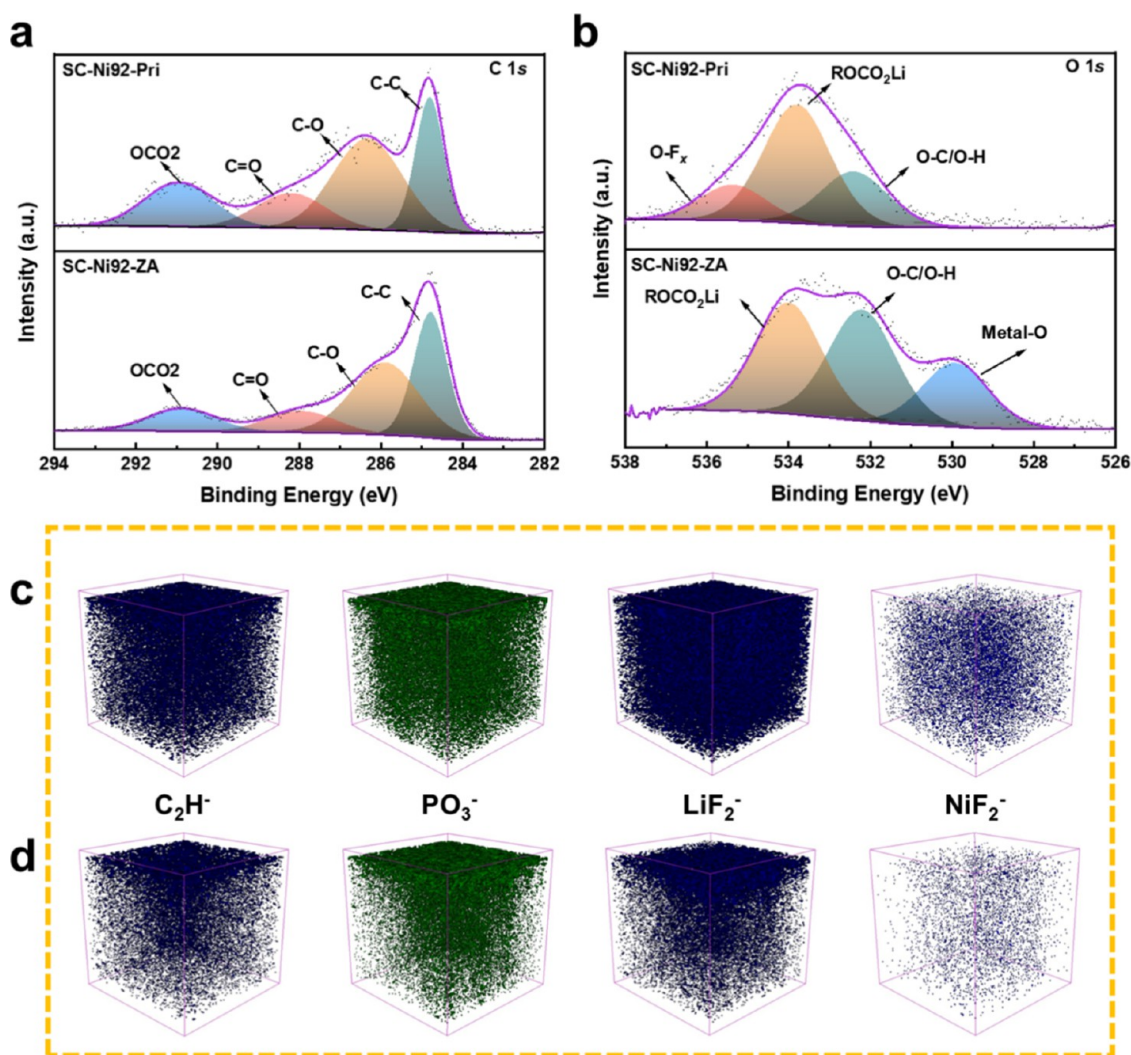
Figure 4. Chemical composition analysis after 200 cycles at 1C within the voltage range of 2.75−4.4 V. XPS spectra and the corresponding fitting results of (a) C 1s and (b) O 1s for SC-Ni92-Pri and SC-Ni92-ZA; The reconstructed 3D images of C_2H^-, PO_3^-, LiF_2^- and NiF_2^- fragments for (c) SC-Ni92-Pri and (d) SC-Ni92-ZA.

cycled cathodes (200 cycles). As shown in Figure 4a−b and Figure S24, Supporting Information, the higher intensities of organic species implied severe electrolyte decomposition on the surface of SC-Ni92-Pri compared to SC-Ni92-ZA. The signal intensity of metal-O for SC-Ni92-ZA was much stronger than that of SC-Ni92-Pri, demonstrating that the lattice oxygen on the surface of SC-Ni92-ZA was more stable. Time of flight secondary ion mass spectroscopy (TOF-SIMS) was further employed to delve deeper into the chemical information on the surface of the cycled electrodes. As depicted in Figure 4c−d and Figure S25−26, Supporting Information, the reconstructed 3D images of C_2H^-, PO_3^-, LiF_2^- and NiF_2^- fragments clearly indicated that SC-Ni92-Pri exhibited a much thicker CEI film than SC-Ni92-ZA. Additionally, the leakage current in SC-Ni92-ZA was significantly lower than in SC-Ni92-Pri at both 45 and 60 °C under the fully charged state, further highlighting the effective suppression of interfacial side reactions in SC-Ni92-ZA (Figure S27, Supporting Information).[47] These results demonstrated that the surface high-entropy rock-salt layer can effectively reduce oxygen evolution and interfacial side reactions, thereby enhancing the stability of interfacial chemistry.

The surface structure of the cycled materials (200 cycles at 1C) at the atomic scale was investigated using a high-angle annular dark-field aberration-corrected scanning transmission electron microscope (HAADF-STEM). As shown in Figure 5a, a thick rock-salt layer (~15 nm) and a disordered layered sublayer can be observed on the surface of cycled SC-Ni92-Pri, which blocked the transport of lithium-ion, increased the impedance, and resulted in rapid capacity decay. Besides, the formation of rock-salt and disordered layered structures is accompanied by lattice oxygen loss accelerating electrolyte decomposition. In contrast, only a thin disordered rock-salt layer was observed on the surface of the cycled SC-Ni92-ZA (Figure 5b), resembling that of pristine SC-Ni92-ZA (Figure 1b). Figure 5c−d shows the electron energy loss spectroscopy (EELS) spectra obtained in HAADF-STEM mode. For the O K-edge spectra, the pre-edge peak located around 530 eV arises from the electron transition from the O 1s state to the hybridized states of O 2p and TM 3d orbitals.[48] The reduction in the intensity of the O pre-edge peak is attributed to oxygen vacancy formation.[9] The O pre-edge peak is absent in the surface region for cycled SC-Ni92-Pri (Figure 5c), implying the formation of significant oxygen vacancies. In contrast, cycled SC-Ni92-ZA displayed a clear O pre-edge peak in the
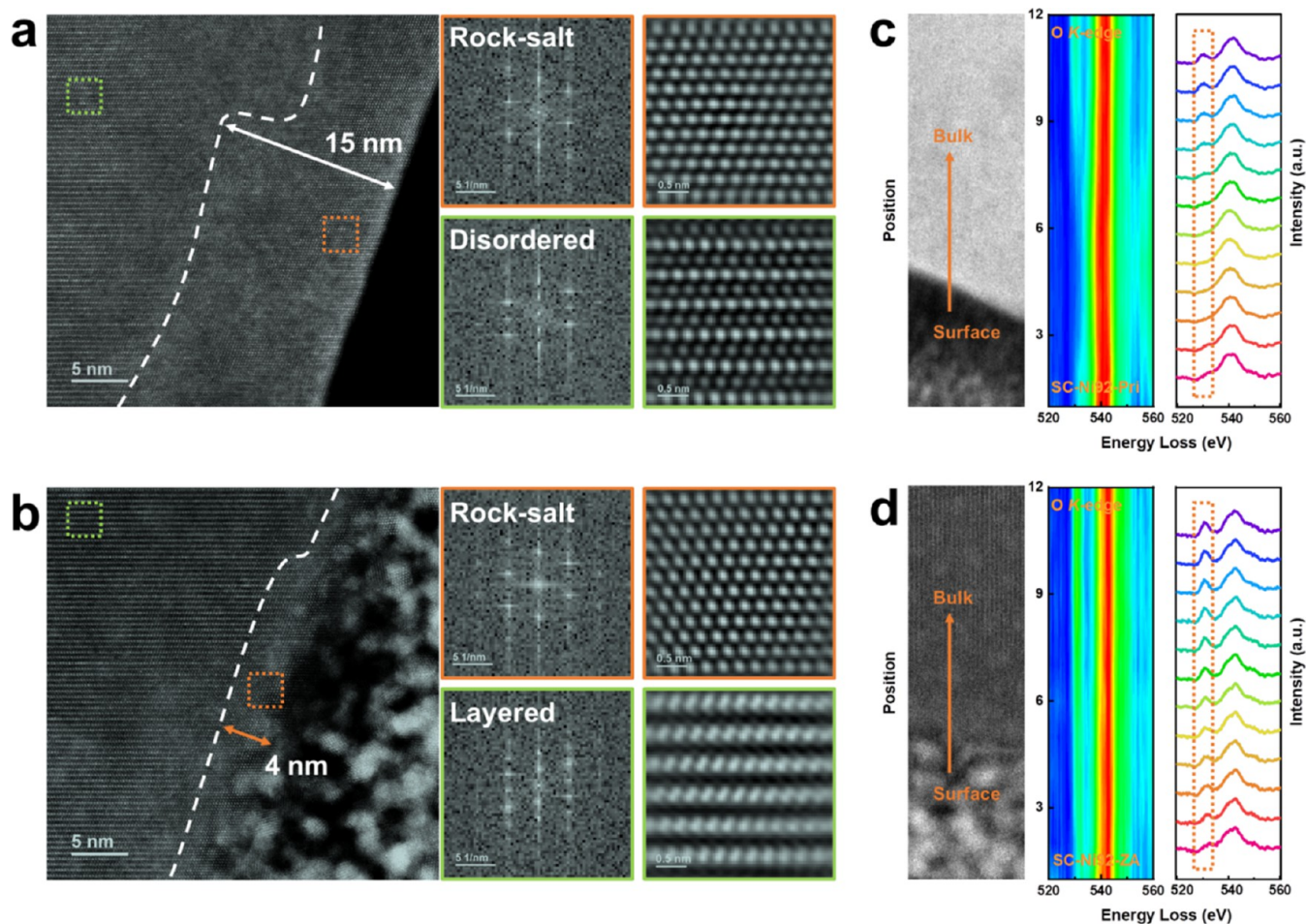
Figure 5. Surface structural degradation. Cross-sectional HAADF-STEM images and the corresponding FFT images of the marked regions for (a) SC-Ni92-Pri and (b) SC-Ni92-ZA cathodes after 200 cycles at 1C within the voltage range of 2.75−4.4 V; The EELS scanning regions and the corresponding spectra of O K-edges for (c) SC-Ni92-Pri and (d) SC-Ni92-ZA.

surface region (Figure 5d), indicating the enhanced stability of near-surface oxygen. On the one hand, the surface high-entropy rock-salt layer effectively stabilizes lattice oxygen. On the other hand, according to Pauling's rules, the increase in highly reactive Ni^{4+} at the near-surface region is suppressed by the introduction of high-valence Zr, enhancing surface structural stability. The surface high-entropy rock-salt layer effectively inhibits unfavorable surface structure degradation and oxygen evolution during cycling, contributing to the maintenance of excellent electrochemical performance.

The schematic diagram illustrating the formation mechanism and evolution of surface structure is shown in Figure 6. Through *in situ* Zr/Al dual-modification, an epitaxial high-entropy rock-salt layer with Ni valence tailored on the surface can be successfully constructed following Pauling's rule of electroneutrality (Figure 6a). Benefiting from the entropy stabilization effect and a lattice-coherent structure, SC-Ni92-ZA retains its layered structure and maintains excellent electrochemical performance even after prolonged cycling. In contrast, SC-Ni92-Pri faces significant challenges, including the formation of a thickened CEI layer, structural deterioration, and microcracking, which ultimately results in rapid capacity decay (Figure 6b).

2. CONCLUSIONS

In summary, we introduced Zr and Al onto the surface of the ultrahigh-Ni single-crystal $LiNi_{0.92}Co_{0.05}Mn_{0.03}O_2$ via *in situ* modification, thereby constructing an epitaxial lattice-coherent high-entropy rock-salt coating layer and realizing near-surface penetration doping of foreign ions. The results of electrochemical tests, structural characterizations, and corresponding DFT calculations demonstrate that the surface high-entropy modification not only protects the interface—by inhibiting lattice oxygen loss, mitigating interface side reactions, and reducing electrolyte decomposition—but also enhances lithium-ion diffusion, stabilizes H2−H3 phase transition, and prevents adverse structural degradation. Consequently, SC-Ni92-ZA exhibits improved and sustained reversible capacity release, maintaining noteworthy enhancements in cycling and rate performance, even under extreme conditions such as high temperature, elevated cutoff voltage, and high rates. In full-cell operation, SC-Ni92-ZA achieved a reversible discharge specific capacity of 169.0 mAh g^{-1} after 600 cycles at 1C, with a capacity retention rate of 87.1%. This work presents a practical approach for enhancing the energy density and lifespan of ultrahigh-Ni single-crystal materials.

3. EXPERIMENTAL SECTION

3.1. Material Synthesis. Commercial $LiNi_{0.92}Co_{0.05}Mn_{0.03}O_2$ (SC-Ni92-Pri) powders were purchased from BAK Power Battery
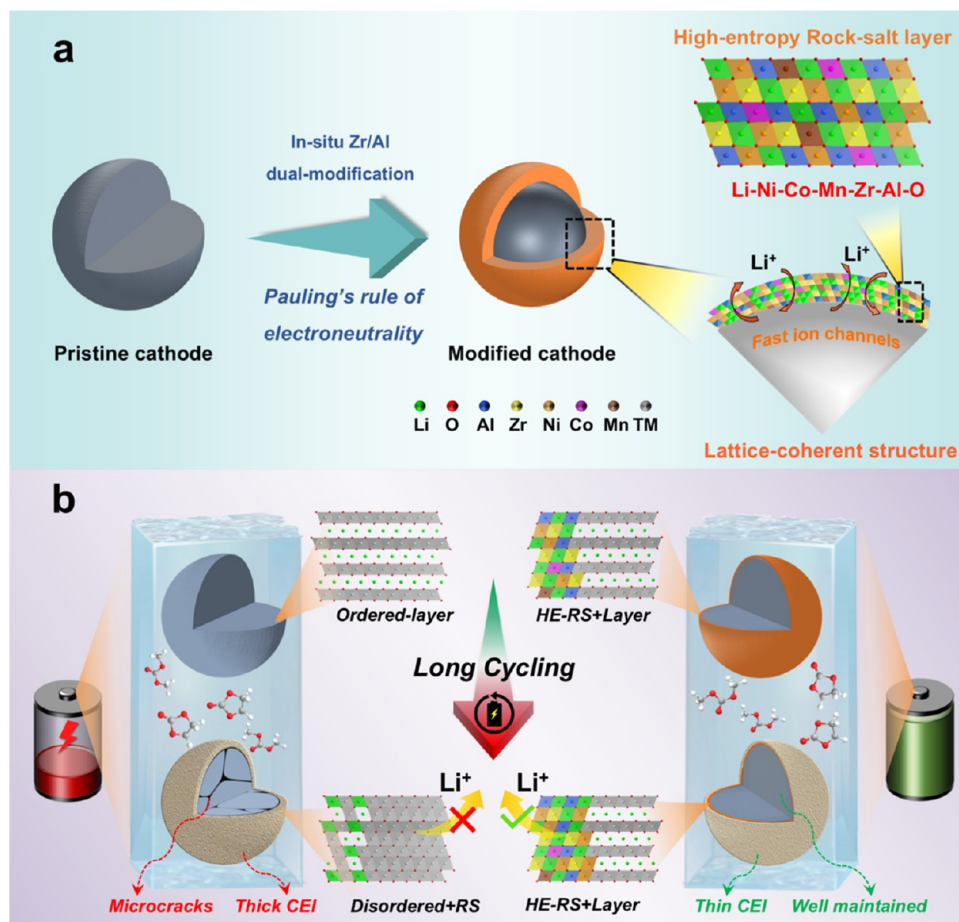
Figure 6. Schematic diagram of the (a) formation mechanism and (b) evolution of surface structure.

Co., Ltd. (Shenzhen, China). Zr and Al surface dual-modified $LiNi_{0.92}Co_{0.05}Mn_{0.03}O_2$ (SC-Ni92-ZA) was prepared through wet mixing and one-step annealing. 1.00 g SC-Ni92-Pri, 0.003 g Zirconium oxynitrate hydrate (99.9%, Innochem), and 0.0021 g $Al(OH)C_4H_6O_4$ (AR, Aladdin) were dispersed in ethanol absolute and ground evenly until the solvent evaporated. Then the mixture was annealed at 500 °C for 5 h in an O_2 atmosphere to obtain the SC-Ni92-ZA.

3.2. Morphological and Structural Characterization. The morphologies of the samples were observed by scanning electron microscope (SEM, Zeiss-SUPRA-55), and the corresponding elemental distribution was investigated using the X-Max EDS detector. The transmission electron microscopy (TEM) imaging was acquired on a field-emission transmission electron microscope (FETEM, JEOL-3200FS) with an accelerating voltage of 300 kV. The cross-sectional information was obtained from the slices of focused ion beam (FIB, FEI-Scios) with liquid Ga as the ion source. The atomic structural imaging and EELS mapping imaging were detected by high-angle annular dark-field scanning transmission electron microscope (HAADF-STEM, JEM-ARM300F). The X-ray diffraction (XRD) results were collected on a Bruker D8 high-resolution X-ray diffractometer with Cu−Kα as the radiation source and the Rietveld refinements of XRD patterns were calculated by GSAS-II software.[49] The surface chemical information on samples was researched by X-ray photoelectron spectrometer (XPS, Thermo Fisher-ESCALAB 250Xi). Time-of-flight secondary-ion mass spectrometry (TOF-SIMS, PHI NanoTOFII) was measured to reveal the chemical information on CEI.

3.3. Electrochemical Measurements. To fabricate the cathode electrode, SC-Ni92 (80 wt %), acetylene black (10 wt %), and polyvinylidene fluoride (PVDF, 10 wt %) were mixed in *N*-methyl-2-pyrrolidone (NMP). The obtained slurry was cast onto the carbon-coated aluminum foil and then dried at 120 °C in a vacuum oven for over 12 h. The mass loading of active materials in the electrodes film was ≈2 mg cm^{-2} and the cathodes were assessed by coin-type (CR2032) cells with metal Li in half-cells or graphite in full cells as anodes, Celgard 2400 polypropylene (PP) membrane as the separator, and 1.0 M $LiPF_6$ dissolved in a 1:1:1 volume ratio of ethylene carbonate: ethyl methyl carbonate: dimethyl carbonate with a 5% vinylene carbonate additive as the electrolyte. The galvanostatic electrochemical tests, galvanostatic intermittent titration technique (GITT), and floating charge tests were performed on the NEWARE battery test system (CT-4008T-5 V10 mA-164). Regarding the floating charge, the cells were charged to 4.4 V at a current density of 100 mA g^{-1} (at temperatures of 45 or 60 °C), and then held at 4.4 V for 120 h to measure the leakage currents. The electrochemical impedance spectroscopy (EIS) and cyclic voltammetry (CV) were carried out on an electrochemical workstation (Solartron Analytical 1470E).

3.4. Computer Details. All density functional calculations were performed with the projector-augmented wave (PAW) method and Perdew−Burke−Ernzerhof (PBE) exchange correlation potential by Vienna ab initio simulation package (VASP).[50−55] The plane-wave energy cutoff was set as 520 eV, and the criterion for electronic energy convergence was set to 10^{-5} eV, respectively. γ-centered Monkhorst−Pack k-point grid sampling was used for the Brillouin zone with a density of at least 1000/(the number of atoms per cell) in all geometry relaxation and self-consistent calculations. Geometries were relaxed until the forces on the atoms were less than 0.02 eV/Å. To account for the strong correlation of transition metal d-electrons, the PBE + U method was used in the calculations to correctly characterize the localization properties,[56,57] with the Hubbard U parameters for Ni, Co, Mn was set as 6.2, 3.3, and 3.9 eV, respectively.[58,59] Spin-polarization was considered in all calculations with the initial magnetic

orders of TMs set to ferromagnetic. The migration barriers of Li-ion were calculated using the method of climbing image nudged elastic band (CI-NEB),[60] and the pathways were optimized until the maximum force was less than 0.03 eV/Å. To examine the influences of Zr and Al doping toward the thermodynamic stability of lattice oxygen and Li-ion diffusion barriers, we built supercells containing 32 $LiMO_2$ formula. For pristine NCM, the chemical formula is $Li_{32}Ni_{29}Co_2MnO_{64}$, and for the half-lithiated state is $Li_{16}Ni_{29}Co_2MnO_{64}$. Ni would be replaced by Al and Zr to estimate the model of Al and Zr near-surface doping, respectively. The oxygen vacancy formation energy is defined as

$$V_O = E(Li_xM_yO_{2-\delta}) + \frac{\delta}{2}E(O_2) - E(Li_xM_yO_2) \tag{1}$$

where $E(Li_xM_yO_{2-\delta})$ and $E(Li_xM_yO_2)$ are the internal energies of the supercell with oxygen vacancy and without oxygen vacancy, respectively. (O_2) is the internal energy of oxygen. A -1.36 eV energy correction for the O_2 molecule was obtained to correct self-interaction errors within GGA calculations.[58]

ASSOCIATED CONTENT

Ⓢ Supporting Information

The Supporting Information is available free of charge at https://pubs.acs.org/doi/10.1021/acsnano.4c13911.

Characterizations of the cathode materials such as SEM, EDS, XRD, XPS, and TOF-SIMS before or after cycling; electrochemical characterizations such as cycle and rate performance, EIS, CV, and GITT; DFT calculations of oxygen vacancy formation energy and lithium-ion migration energy barrier; leakage current during float charging test (PDF)

AUTHOR INFORMATION

Corresponding Authors

Jiajie Liu − *School of Advanced Materials, Peking University, Shenzhen Graduate School, Shenzhen 518055, P. R. China*; Email: liujiajie@sz.pku.edu.cn

Xinghua Tan − *School of Advanced Materials, Peking University, Shenzhen Graduate School, Shenzhen 518055, P. R. China; Shenyang National Laboratory for Materials Science, Institute of Metal Research, Chinese Academy of Sciences, Shenyang 110016, P. R. China*; Email: xhtan@imr.ac.cn

Feng Pan − *School of Advanced Materials, Peking University, Shenzhen Graduate School, Shenzhen 518055, P. R. China*; ⓞ orcid.org/0000-0002-8216-1339; Email: panfeng@pkusz.edu.cn

Authors

Zhongxing Xu − *School of Advanced Materials, Peking University, Shenzhen Graduate School, Shenzhen 518055, P. R. China; School of Materials Science and Engineering, Shanghai Jiao Tong University, Shanghai 200240, P. R. China*

Xinghan Chen − *School of Advanced Materials, Peking University, Shenzhen Graduate School, Shenzhen 518055, P. R. China; School of Materials, Sun Yat-sen University, Shenzhen 518107, P. R. China*

Wenguang Fan − *School of Advanced Materials, Peking University, Shenzhen Graduate School, Shenzhen 518055, P. R. China*

Minzhi Zhan − *School of Advanced Materials, Peking University, Shenzhen Graduate School, Shenzhen 518055, P. R. China*

Xulin Mu − *Shenyang National Laboratory for Materials Science, Institute of Metal Research, Chinese Academy of Sciences, Shenyang 110016, P. R. China*

Hongbin Cao − *School of Advanced Materials, Peking University, Shenzhen Graduate School, Shenzhen 518055, P. R. China*

Xiaohu Wang − *School of Advanced Materials, Peking University, Shenzhen Graduate School, Shenzhen 518055, P. R. China*

Haoyu Xue − *School of Advanced Materials, Peking University, Shenzhen Graduate School, Shenzhen 518055, P. R. China*

Zhihai Gao − *School of Advanced Materials, Peking University, Shenzhen Graduate School, Shenzhen 518055, P. R. China*

Yongzhi Liang − *School of Advanced Materials, Peking University, Shenzhen Graduate School, Shenzhen 518055, P. R. China*

Complete contact information is available at:
https://pubs.acs.org/10.1021/acsnano.4c13911

Author Contributions

[⊥]Z.X., X.C., and W.F. contributed equally to this work.

Notes

The authors declare no competing financial interest.

ACKNOWLEDGMENTS

ABBREVIATIONS

SC-Ni92-Pri, pristine ultrahigh-Ni single-crystalline cathode $LiNi_{0.92}Co_{0.05}Mn_{0.03}O_2$; SC-Ni92-ZA, the high-entropy surface-layer-stabilized ultrahigh-Ni single-crystalline cathode; NCM, $LiNi_xCo_yMn_{1-x-y}O_2$; SOCs, states of charge; CEI, cathode electrolyte interface

REFERENCES

(1) Mao, M.; Ji, X.; Wang, Q.; Lin, Z.; Li, M.; Liu, T.; Wang, C.; Hu, Y.-S.; Li, H.; Huang, X.; Chen, L.; Suo, L. Anion-Enrichment Interface Enables High-Voltage Anode-Free Lithium Metal Batteries. *Nat. Commun.* **2023**, *14* (1), No. 1082.

(2) Park, S.; Jeong, S. Y.; Lee, T. K.; Park, M. W.; Lim, H. Y.; Sung, J.; Cho, J.; Kwak, S. K.; Hong, S. Y.; Choi, N.-S. Replacing Conventional Battery Electrolyte Additives with Dioxolone Derivatives for High-Energy-Density Lithium-Ion Batteries. *Nat. Commun.* **2021**, *12* (1), No. 838.

(3) Kim, U.-H.; Park, G.-T.; Son, B.-K.; Nam, G. W.; Liu, J.; Kuo, L.-Y.; Kaghazchi, P.; Yoon, C. S.; Sun, Y.-K. Heuristic Solution for Achieving Long-Term Cycle Stability for Ni-Rich Layered Cathodes at Full Depth of Discharge. *Nat. Energy* **2020**, *5* (11), 860−869.

(4) Liu, Y.; Zeng, T.; Li, G.; Wan, T.; Li, M.; Zhang, X.; Li, M.; Su, M.; Dou, A.; Zeng, W.; Zhou, Y.; Guo, R.; Chu, D. The Surface Double-Coupling on Single-Crystal $LiNi_{0.8}Co_{0.1}Mn_{0.1}O_2$ for Inhibiting

the Formation of Intragranular Cracks and Oxygen Vacancies. *Energy Storage Mater.* **2022**, *52*, 534−546.

(5) Hu, J.; Wang, H.; Xiao, B.; Liu, P.; Huang, T.; Li, Y.; Ren, X.; Zhang, Q.; Liu, J.; Ouyang, X.; Sun, X. Challenges and Approaches of Single-Crystal Ni-Rich Layered Cathodes in Lithium Batteries. *Natl. Sci. Rev.* **2023**, *10* (12), No. nwad252.

(6) Jiang, M.; Danilov, D. L.; Eichel, R.; Notten, P. H. L. A Review of Degradation Mechanisms and Recent Achievements for Ni-Rich Cathode-Based Li-Ion Batteries. *Adv. Energy Mater.* **2021**, *11* (48), No. 2103005.

(7) Tan, S.; Shadike, Z.; Li, J.; Wang, X.; Yang, Y.; Lin, R.; Cresce, A.; Hu, J.; Hunt, A.; Waluyo, I.; Ma, L.; Monaco, F.; Cloetens, P.; Xiao, J.; Liu, Y.; Yang, X.-Q.; Xu, K.; Hu, E. Additive Engineering for Robust Interphases to Stabilize High-Ni Layered Structures at Ultra-High Voltage of 4.8 V. *Nat. Energy* **2022**, *7* (6), 484−494.

(8) Wang, C.; Wang, X.; Zhang, R.; Lei, T.; Kisslinger, K.; Xin, H. L. Resolving Complex Intralayer Transition Motifs in High-Ni-Content Layered Cathode Materials for Lithium-Ion Batteries. *Nat. Mater.* **2023**, *22* (2), 235−241.

(9) Qi, M.; Zhang, S.; Guo, S.; Ji, P.; Mao, J.; Wu, T.; Lu, S.; Zhang, X.; Chen, S.; Su, D.; Chen, G.; Cao, A. Integrated Surface Modulation of Ultrahigh Ni Cathode Materials for Improved Battery Performance. *Small Methods* **2023**, *7* (7), No. 2300280.

(10) Ryu, H.-H.; Namkoong, B.; Kim, J.-H.; Belharouak, I.; Yoon, C. S.; Sun, Y.-K. Capacity Fading Mechanisms in Ni-Rich Single-Crystal NCM Cathodes. *ACS Energy Lett.* **2021**, *6* (8), 2726−2734.

(11) Wang, C.; Zhang, R.; Siu, C.; Ge, M.; Kisslinger, K.; Shin, Y.; Xin, H. L. Chemomechanically Stable Ultrahigh-Ni Single-Crystalline Cathodes with Improved Oxygen Retention and Delayed Phase Degradations. *Nano Lett.* **2021**, *21* (22), 9797−9804.

(12) Wang, C.; Han, L.; Zhang, R.; Cheng, H.; Mu, L.; Kisslinger, K.; Zou, P.; Ren, Y.; Cao, P.; Lin, F.; Xin, H. L. Resolving Atomic-Scale Phase Transformation and Oxygen Loss Mechanism in Ultrahigh-Nickel Layered Cathodes for Cobalt-Free Lithium-Ion Batteries. *Matter* **2021**, *4* (6), 2013−2026.

(13) Wang, C.; Wang, X.; Zou, P.; Zhang, R.; Wang, S.; Song, B.; Low, K.-B.; Xin, H. L. Direct Observation of Chemomechanical Stress-Induced Phase Transformation in High-Ni Layered Cathodes for Lithium-Ion Batteries. *Matter* **2023**, *6* (4), 1265−1277.

(14) Wang, C.; Jing, Y.; Zhu, D.; Xin, H. L. Atomic Origin of Chemomechanical Failure of Layered Cathodes in All-Solid-State Batteries. *J. Am. Chem. Soc.* **2024**, *146* (26), 17712−17718.

(15) Zheng, W.; Liang, G.; Liu, Q.; Li, J.; Yuwono, J. A.; Zhang, S.; Peterson, V. K.; Guo, Z. The Promise of High-Entropy Materials for High-Performance Rechargeable Li-Ion and Na-Ion Batteries. *Joule* **2023**, *7* (12), 2732−2748.

(16) Gao, H.; Li, J.; Zhang, F.; Li, C.; Xiao, J.; Nie, X.; Zhang, G.; Xiao, Y.; Zhang, D.; Guo, X.; Wang, Y.; Kang, Y.; Wang, G.; Liu, H. Revealing the Potential and Challenges of High-Entropy Layered Cathodes for Sodium-Based Energy Storage. *Adv. Energy Mater.* **2024**, *14* (20), No. 2304529.

(17) Huang, L.; Zhu, J.; Liu, J.-X.; Wu, H.; Zhang, G.-J. The Emerging High-Entropy Strategy: A Booster to the Development of Cathode Materials for Power Batteries. *J. Adv. Ceram.* **2024**, *13*, 1093.

(18) Huang, H.; Zhao, J.; Guo, H.; Weng, B.; Zhang, H.; Saha, R. A.; Zhang, M.; Lai, F.; Zhou, Y.; Juan, R.; Chen, P.; Wang, S.; Steele, J. A.; Zhong, F.; Liu, T.; Hofkens, J.; Zheng, Y.; Long, J.; Roeffaers, M. B. J. Noble-Metal-Free High-Entropy Alloy Nanoparticles for Efficient Solar-Driven Photocatalytic CO_2 Reduction. *Adv. Mater.* **2024**, *36* (26), No. 2313209.

(19) Wang, J.; Cui, Y.; Wang, Q.; Wang, K.; Huang, X.; Stenzel, D.; Sarkar, A.; Azmi, R.; Bergfeldt, T.; Bhattacharya, S. S.; Kruk, R.; Hahn, H.; Schweidler, S.; Brezesinski, T.; Breitung, B. Lithium Containing Layered High Entropy Oxide Structures. *Sci. Rep* **2020**, *10* (1), No. 18430.

(20) Yang, Y.; Cai, J.; Zuo, Y.; Zhang, K.; Gao, C.; Zhou, L.; Chen, Z.; Chu, W.; Xia, D. Enhancing the Stability of Li-Rich Mn-Based Oxide Cathodes through Surface High-Entropy Strategy. *Energy Storage Mater.* **2024**, *71*, No. 103587.

(21) Song, J.; Ning, F.; Zuo, Y.; Li, A.; Wang, H.; Zhang, K.; Yang, T.; Yang, Y.; Gao, C.; Xiao, W.; Jiang, Z.; Chen, T.; Feng, G.; Xia, D. Entropy Stabilization Strategy for Enhancing the Local Structural Adaptability of Li-Rich Cathode Materials. *Adv. Mater.* **2023**, *35* (7), No. 2208726.

(22) Zhao, C.; Wang, C.; Liu, X.; Hwang, I.; Li, T.; Zhou, X.; Diao, J.; Deng, J.; Qin, Y.; Yang, Z.; Wang, G.; Xu, W.; Sun, C.; Wu, L.; Cha, W.; Robinson, I.; Harder, R.; Jiang, Y.; Bicer, T.; Li, J.-T.; Lu, W.; Li, L.; Liu, Y.; Sun, S.-G.; Xu, G.-L.; Amine, K. Suppressing Strain Propagation in Ultrahigh-Ni Cathodes during Fast Charging via Epitaxial Entropy-Assisted Coating. *Nat. Energy* **2024**, *9* (3), 345−356.

(23) Wang, B.; Ma, J.; Wang, K.; Wang, D.; Xu, G.; Wang, X.; Hu, Z.; Pao, C.; Chen, J.; Du, L.; Du, X.; Cui, G. High-Entropy Phase Stabilization Engineering Enables High-Performance Layered Cathode for Sodium-Ion Batteries. *Adv. Energy Mater.* **2024**, *14* (23), No. 2401090.

(24) Zhang, R.; Wang, C.; Zou, P.; Lin, R.; Ma, L.; Li, T.; Hwang, I.; Xu, W.; Sun, C.; Trask, S.; Xin, H. L. Long-Life Lithium-Ion Batteries Realized by Low-Ni, Co-Free Cathode Chemistry. *Nat. Energy* **2023**, *8* (7), 695−702.

(25) Zhang, R.; Wang, C.; Zou, P.; Lin, R.; Ma, L.; Yin, L.; Li, T.; Xu, W.; Jia, H.; Li, Q.; Sainio, S.; Kisslinger, K.; Trask, S. E.; Ehrlich, S. N.; Yang, Y.; Kiss, A. M.; Ge, M.; Polzin, B. J.; Lee, S. J.; Xu, W.; Ren, Y.; Xin, H. L. Compositionally Complex Doping for Zero-Strain Zero-Cobalt Layered Cathodes. *Nature* **2022**, *610* (7930), 67−73.

(26) Tan, X.; Zhang, Y.; Xu, S.; Yang, P.; Liu, T.; Mao, D.; Qiu, J.; Chen, Z.; Lu, Z.; Pan, F.; Chu, W. High-Entropy Surface Complex Stabilized $LiCoO_2$ Cathode. *Adv. Energy Mater.* **2023**, *13* (24), No. 2300147.

(27) Huang, Y.; Liu, L.; Zhu, Y.; Gao, M.; Zhang, J. A New Model on Cation Distribution in Cation-Disordered $Li_{1+x}TM_{1−x}O_2$ Cathodes. *Solid State Ionics* **2020**, *351*, No. 115341.

(28) George, J.; Waroquiers, D.; Di Stefano, D.; Petretto, G.; Rignanese, G.; Hautier, G. The Limited Predictive Power of the Pauling Rules. *Angew. Chem., Int. Ed* **2020**, *59* (19), 7569−7575.

(29) Wu, F.; Liu, N.; Chen, L.; Li, N.; Lu, Y.; Cao, D.; Xu, M.; Wang, Z.; Su, Y. A Universal Method for Enhancing the Structural Stability of Ni-Rich Cathodes Via the Synergistic Effect of Dual-Element Cosubstitution. *ACS Appl. Mater. Interfaces* **2021**, *13* (21), 24925−24936.

(30) Wu, F.; Liu, N.; Chen, L.; Su, Y.; Tan, G.; Bao, L.; Zhang, Q.; Lu, Y.; Wang, J.; Chen, S.; Tan, J. Improving the Reversibility of the H2-H3 Phase Transitions for Layered Ni-Rich Oxide Cathode towards Retarded Structural Transition and Enhanced Cycle Stability. *Nano Energy* **2019**, *59*, 50−57.

(31) Tian, J.; Wang, G.; Zeng, W.; Zhu, J.; Tian, W.; Zhang, S.; Zhang, Y.; Wang, J.; Li, Q.; Zhao, H.; Li, C.; Li, X.; Chen, L.; Mu, S. A Bimetal Strategy for Suppressing Oxygen Release of 4.6V High-Voltage Single-Crystal High-Nickel Cathode. *Energy Storage Mater.* **2024**, *68*, No. 103344.

(32) Sim, R.; Cui, Z.; Manthiram, A. Impact of Dopants on Suppressing Gas Evolution from High-Nickel Layered Oxide Cathodes. *ACS Energy Lett.* **2023**, *8* (12), 5143−5148.

(33) Wang, G.; Xie, C.; Wang, H.; Li, Q.; Xia, F.; Zeng, W.; Peng, H.; Van Tendeloo, G.; Tan, G.; Tian, J.; Wu, J. Mitigated Oxygen Loss in Lithium-Rich Manganese-Based Cathode Enabled by Strong Zr−O Affinity. *Adv. Funct Mater.* **2024**, *34* (23), No. 2313672.

(34) Jiang, M.; Danilov, D. L.; Eichel, R.; Notten, P. H. L. A Review of Degradation Mechanisms and Recent Achievements for Ni-Rich Cathode-Based Li-Ion Batteries. *Adv. Energy Mater.* **2021**, *11* (48), No. 2103005.

(35) P S, J.; Sutrave, D. S. A Brief Study of Cyclic Voltammetry and Electrochemical Analysis. *IJCTR* **2018**, *11* (9), 77−88.

(36) Chu, Y.; Mu, Y.; Zou, L.; Hu, Y.; Cheng, J.; Wu, B.; Han, M.; Xi, S.; Zhang, Q.; Zeng, L. Thermodynamically Stable Dual-Modified $LiF\&FeF_3$ Layer Empowering Ni-Rich Cathodes with Superior Cyclabilities. *Adv. Mater.* **2023**, *35* (21), No. 2212308.

(37) Du, Y.; Fujita, K.; Shironita, S.; Sone, Y.; Hosono, E.; Asakura, D.; Umeda, M. Capacity Fade Characteristics of Nickel-Based Lithium-Ion Secondary Battery after Calendar Deterioration at 80 °C. *J. Power Sources* **2021**, *501*, No. 230005.

(38) Xu, L.; Xiao, Y.; Yang, Y.; Yang, S.; Chen, X.; Xu, R.; Yao, Y.; Cai, W.; Yan, C.; Huang, J.; Zhang, Q. *Operando* Quantified Lithium Plating Determination Enabled by Dynamic Capacitance Measurement in Working Li-Ion Batteries. *Angew. Chem., Int. Ed* **2022**, *61* (39), No. e202210365.

(39) He, R.; He, Y.; Xie, W.; Guo, B.; Yang, S. Comparative Analysis for Commercial Li-Ion Batteries Degradation Using the Distribution of Relaxation Time Method Based on Electrochemical Impedance Spectroscopy. *Energy* **2023**, *263*, No. 125972.

(40) Lu, Y.; Zhao, C.-Z.; Zhang, R.; Yuan, H.; Hou, L.-P.; Fu, Z.-H.; Chen, X.; Huang, J.-Q.; Zhang, Q. The Carrier Transition from Li Atoms to Li Vacancies in Solid-State Lithium Alloy Anodes. *Sci. Adv.* **2021**, *7* (38), No. eabi5520.

(41) Lu, Y.; Zhao, C.-Z.; Huang, J.-Q.; Zhang, Q. The Timescale Identification Decoupling Complicated Kinetic Processes in Lithium Batteries. *Joule* **2022**, *6* (6), 1172−1198.

(42) Li, F.; Liu, Z.; Liao, C.; Xu, X.; Zhu, M.; Liu, J. Gradient Boracic Polyanion Doping-Derived Surface Lattice Modulation of High-Voltage Ni-Rich Layered Cathodes for High-Energy-Density Li-Ion Batteries. *ACS Energy Lett.* **2023**, *8* (11), 4903−4914.

(43) Lu, S.-j.; Tang, L.; Wei, H.; Huang, Y.; Yan, C.; He, Z.; Li, Y.; Mao, J.; Dai, K.; Zheng, J. Single-Crystal Nickel-Based Cathodes: Fundamentals and Recent Advances. *Electrochem. Energy Rev.* **2022**, *5* (4), No. 15.

(44) Liao, C.; Li, F.; Liu, J. Challenges and Modification Strategies of Ni-Rich Cathode Materials Operating at High-Voltage. *Nanomaterials* **2022**, *12* (11), 1888.

(45) Xu, M.; Sheng, B.; Cheng, Y.; Lu, J.; Chen, M.; Wang, P.; Liu, B.; Chen, J.; Han, X.; Wang, M.-S.; Shi, S. One-Step Calcination Synthesis of Interface-Coherent Crystallized and Surface-Passivated $LiNi_{0.5}Mn_{1.5}O_4$ for High-Voltage Lithium-Ion Battery. *Nano Res.* **2024**, *17* (5), 4192−4202.

(46) Fan, X.; Hu, G.; Zhang, B.; Ou, X.; Zhang, J.; Zhao, W.; Jia, H.; Zou, L.; Li, P.; Yang, Y. Crack-Free Single-Crystalline Ni-Rich Layered NCM Cathode Enable Superior Cycling Performance of Lithium-Ion Batteries. *Nano Energy* **2020**, *70*, No. 104450.

(47) Zhang, Z.; Hu, L.; Wu, H.; Weng, W.; Koh, M.; Redfern, P. C.; Curtiss, L. A.; Amine, K. Fluorinated Electrolytes for 5 V Lithium-Ion Battery Chemistry. *Energy Environ. Sci.* **2013**, *6* (6), 1806.

(48) Park, H.; Mesnier, A.; Lee, S.; Jarvis, K.; Manthiram, A.; Warner, J. H. Intrinsic Li Distribution in Layered Transition-Metal Oxides Using Low-Dose Scanning Transmission Electron Microscopy and Spectroscopy. *Chem. Mater.* **2021**, *33* (12), 4638−4650.

(49) Toby, B. H.; Von Dreele, R. B. *GSAS-II*: The Genesis of a Modern Open-Source All Purpose Crystallography Software Package. *J. Appl. Crystallogr.* **2013**, *46* (2), 544−549.

(50) Kresse, G.; Hafner, J. *Ab Initio* Molecular Dynamics for Liquid Metals. *Phys. Rev. B* **1993**, *47* (1), 558−561.

(51) Kresse, G.; Furthmüller, J. Efficiency of Ab-Initio Total Energy Calculations for Metals and Semiconductors Using a Plane-Wave Basis Set. *Comput. Mater. Sci.* **1996**, *6* (1), 15−50.

(52) Mishra, S. K.; Ceder, G. Structural Stability of Lithium Manganese Oxides. *Phys. Rev. B* **1999**, *59* (9), 6120−6130.

(53) Blöchl, P. E. Projector Augmented-Wave Method. *Phys. Rev. B* **1994**, *50* (24), 17953−17979.

(54) Kresse, G.; Joubert, D. From Ultrasoft Pseudopotentials to the Projector Augmented-Wave Method. *Phys. Rev. B* **1999**, *59* (3), 1758−1775.

(55) Perdew, J. P.; Burke, K.; Ernzerhof, M. Generalized Gradient Approximation Made Simple. *Phys. Rev. Lett.* **1996**, *77* (18), 3865−3868.

(56) Dudarev, S. L.; Botton, G. A.; Savrasov, S. Y.; Humphreys, C. J.; Sutton, A. P. Electron-Energy-Loss Spectra and the Structural Stability of Nickel Oxide: An LSDA + U Study. *Phys. Rev. B* **1998**, *57* (3), 1505−1509.

(57) Anisimov, V. I.; Zaanen, J.; Andersen, O. K. Band Theory and Mott Insulators: Hubbard *U* Instead of Stoner *I*. *Phys. Rev. B* **1991**, *44* (3), 943−954.

(58) Wang, L.; Maxisch, T.; Ceder, G. Oxidation Energies of Transition Metal Oxides within the GGA + U Framework. *Phys. Rev. B* **2006**, *73* (19), No. 195107.

(59) Liu, M.; Rong, Z.; Malik, R.; Canepa, P.; Jain, A.; Ceder, G.; Persson, K. A. Spinel Compounds as Multivalent Battery Cathodes: A Systematic Evaluation Based on Ab Initio Calculations. *Energy Environ. Sci.* **2015**, *8* (3), 964−974.

(60) Henkelman, G.; Uberuaga, B. P.; Jónsson, H. A Climbing Image Nudged Elastic Band Method for Finding Saddle Points and Minimum Energy Paths. *J. Chem. Phys.* **2000**, *113* (22), 9901−9904.